

---

# Probability-Flow Distillation: Exact Wasserstein Gradient Flow for High-Fidelity 3D Generation

---

**Rohith Ramanan**

Department of Physics  
Indian Institute of Technology Madras  
rrohith2633@gmail.com

**A. N. Rajagopalan**

Department of Electrical Engineering  
Indian Institute of Technology Madras  
raju@ee.iitm.ac.in

## Abstract

Score Distillation Sampling (SDS) and its variants have been widely used for text-to-3D generation by distilling 2D image diffusion priors. However, the standard SDS objective is prone to severe mode collapse, frequently yielding over-smoothed and over-saturated results. Although recent advancements, such as Score Distillation via Inversion (SDI), mitigate these artifacts and produce visually sharper models, they ultimately fail to faithfully capture the full target distribution. In this work, we show that the bottleneck limiting the sampling capacity of SDI stems from its reliance on the posterior mean estimator, which is mathematically equivalent to a single-step Euler approximation of the deterministic reverse DDIM trajectory. To address this, we propose a naturally motivated extension termed Probability-Flow Distillation (PFD). We establish that PFD corresponds exactly to a Wasserstein gradient flow, thereby inducing principled distribution-matching dynamics. Finally, we show that PFD can synthesize 3D assets with fine-grained, high-fidelity details and achieve improved quality compared to existing methods.

## 1 Introduction

Diffusion-based and related generative models [1, 2, 3, 4, 5] have established state-of-the-art performance in realistic image synthesis. However, extension of these capabilities to direct text-to-3D generation remains severely bottlenecked by the lack of large-scale, high-quality 3D training data. To mitigate this data scarcity, the pioneering work DreamFusion [6] introduces Score Distillation Sampling (SDS), which leverages pre-trained 2D diffusion models as implicit priors to optimize parameterized 3D representations [7, 8, 9, 10]. Despite its effectiveness, SDS often produces over-smoothed geometry and textures with unnatural color saturation. Subsequent work has attempted to alleviate these issues through heuristic gradient modifications [11, 12] and multi-stage optimization pipelines [13, 14, 15]. In particular, Classifier Score Distillation (CSD) [16] suggests that the guidance term alone, namely the difference between the text-conditioned and unconditional prediction, is sufficient for effective text-to-3D generation. Despite these refinements, such approaches remain constrained by the fundamental limitations of the SDS gradient.

SDS and its variants recast sampling over the parameters of the underlying representation as an optimization problem. From this perspective, the SDS gradient behaves as a mode-seeking force rather than a true generative sampling mechanism, precipitating the observed artifacts. ProlificDreamer [17] addresses this limitation by framing the problem through the lens of particle variational inference via Variational Score Distillation (VSD), which induces a Wasserstein gradient flow in the space of probability measures, thus promoting distribution matching. However, this formulation requires LoRA-based [18] fine-tuning of the diffusion model, incurring additional memory overhead.

In parallel, Score Distillation with Inversion (SDI) [19] improves the optimization dynamics by reinterpreting the SDS formulation as a high-variance reparameterization of DDIM sampling. By

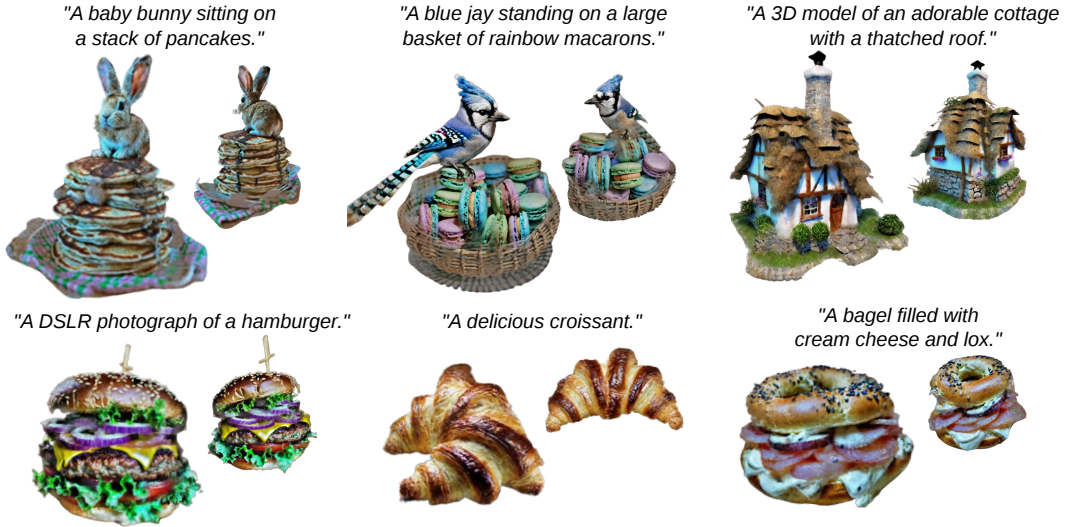


Figure 1: Examples of 3D objects generated using PFD.

replacing random noise additions with deterministic inversion, SDI produces sharper assets with more detailed textures compared to SDS. Nevertheless, SDI remains fundamentally limited in its ability to capture the full structural complexity of the target distribution.

We demonstrate that this limitation of SDI arises from its dependence on the posterior mean estimator, which reduces to a coarse single-step Euler approximation of the reverse diffusion trajectory. This observation motivates a generalization: replacing the biased single-step evaluation with exact integration of the Probability-Flow ODE (PF-ODE). Although SDS-Bridge [20], based on Dual Diffusion Implicit Bridges [21], alludes to a closely related extension, it neither develops this viewpoint into a primary algorithmic approach nor formalizes it as a sampling method. Through this perspective, we additionally provide an interpretation for the use of negative Classifier-Free Guidance scale in SDI.

Building on this observation, we propose *Probability-Flow Distillation* (PFD), a deterministic procedure to sample in parameter space that constructs the gradient by integrating the PF-ODE in both forward and reverse directions. Consistent with previous work (e.g. SDS, VSD), we use the term “distillation” to denote the extraction of information from diffusion models to guide optimization in parameter space, rather than the distillation of student-teacher aimed at accelerating inference. We establish that PFD induces a Wasserstein gradient flow, minimizing a time-averaged KL divergence between the generated and target distributions, enabling distribution alignment.

We extend PFD to text-to-3D using an approximation akin to those implicitly employed in prior work, thereby removing the need for model adaption to learn the score of the current parameter distribution, while preserving performance. PFD produces higher-quality 3D objects (see Figure 1) with improved texture details and visual appeal compared to SDI. Although it incurs additional per-iteration cost due to solving the PF-ODE in both directions, it requires fewer iterations than SDI to achieve better results. Furthermore, PFD achieves visual fidelity similar to or better than VSD while maintaining memory usage comparable to SDI.

In summary, our main contributions are as follows:

- We show that DDIM’s posterior mean estimator corresponds to a coarse single-step Euler discretization of the reverse diffusion trajectory, which limits the sampling capacity of SDI (Section 4).
- We propose Probability-Flow Distillation, replacing this approximation with exact integration of the PF-ODE, and show that this induces a Wasserstein gradient flow and gives rise to a principled sampling procedure (Section 5).
- We apply PFD to text-to-3D generation and demonstrate competitive generation quality relative to state-of-the-art distillation methods (Section 6).

## 2 Preliminaries

**Probability Flow ODE.** Consider the Itô SDE,  $d\mathbf{x}_t = \mathbf{f}(\mathbf{x}_t, t) dt + g(t) d\mathbf{W}_t$ , where  $\mathbf{W}_t$  denotes the standard Brownian motion, and  $p_t(\mathbf{x}_t)$  denotes the marginal density of  $\mathbf{x}_t \in \mathbb{R}^d$ . Anderson [22] derived the corresponding reverse-time SDE:

$$d\mathbf{x}_t = [\mathbf{f}(\mathbf{x}_t, t) - g(t)^2 \nabla_{\mathbf{x}} \log p_t(\mathbf{x}_t)] dt + g(t) d\bar{\mathbf{W}}_t,$$

where  $\bar{\mathbf{W}}_t$  is a reverse-time Brownian motion. The quantity  $\nabla_{\mathbf{x}} \log p_t(\mathbf{x})$ , known as the *score function*, is generally intractable but can be approximated via denoising score matching [23]. By training a neural network  $\epsilon_\phi(\mathbf{x}_t, t)$  to predict the noise injected during the forward process, the score is recovered up to a time-dependent scaling factor, i.e.,  $\nabla_{\mathbf{x}} \log p_t(\mathbf{x}_t) \propto -\epsilon_\phi(\mathbf{x}_t, t)$ . The stochastic dynamics can be recast as a deterministic flow that preserves the same marginal densities  $p_t(\mathbf{x}_t)$  for all  $t$ , provided consistent initial conditions. This yields the *Probability-Flow ODE* (PF-ODE) [24]:

$$\frac{d\mathbf{x}_t}{dt} = \mathbf{f}(\mathbf{x}_t, t) - \frac{1}{2}g(t)^2 \nabla_{\mathbf{x}} \log p_t(\mathbf{x}_t).$$

**Diffusion Models.** Modern diffusion models are commonly formulated via the Variance-Preserving (VP) SDE [24]. The forward diffusion process is defined by the stochastic differential equation:  $d\mathbf{x}_t = -\frac{1}{2}\beta_t \mathbf{x}_t dt + \sqrt{\beta_t} d\mathbf{W}_t$ , where  $\beta_t$  controls the noise schedule. This continuous-time dynamics yields the discrete transition kernel  $\mathbf{x}_t = \sqrt{\alpha_t} \mathbf{x}_0 + \sqrt{1 - \alpha_t} \epsilon$ , where  $\epsilon \sim \mathcal{N}(0, I)$  and  $\alpha_t = \exp(-\int_0^t \beta(s) ds)$ . The PF-ODE linked to this VP-SDE precisely matches the deterministic DDIM-ODE [25].

By introducing the signal-to-noise ratio  $\sigma_t := \sqrt{(1 - \alpha_t)/\alpha_t}$  and a scaled state variable  $\tilde{\mathbf{x}}_t := \mathbf{x}_t / \sqrt{\alpha_t}$ , the forward transition can be simplified to  $\tilde{\mathbf{x}}_t = \mathbf{x}_0 + \sigma_t \epsilon$ . Using this reparameterization, the governing DDIM PF-ODE takes on a remarkably concise form (See Appendix C):

$$\frac{d\tilde{\mathbf{x}}_t}{dt} = \epsilon_\phi(\mathbf{x}_t, t) \frac{d\sigma_t}{dt}, \quad \mathbf{x}_t = \frac{\tilde{\mathbf{x}}_t}{\sqrt{1 + \sigma_t^2}}.$$

The noise-prediction network  $\epsilon_\phi(\mathbf{x}_t, t)$  is trained using the standard score-matching objective  $\mathbb{E}_{\mathbf{x}_0, \epsilon, t} [\|\epsilon - \epsilon_\phi(\mathbf{x}_t, t)\|^2]$ . Given the deterministic nature of the DDIM-ODE, the backward-time integration (i.e. from  $t = 0$  to  $t = T$ ) uniquely maps a clean observation  $\mathbf{x}_0$  to its corresponding noise representation  $\mathbf{x}_T$ . This technique, commonly referred to as DDIM inversion [26, 27], serves as the foundational mechanism for numerous text-guided image editing methodologies.

**Wasserstein Gradient Flows.** We consider  $\mathcal{P}_2(\mathbb{R}^d)$ , the space of Borel probability measures possessing a finite second moment, endowed with the 2-Wasserstein metric  $W_2$ . For a given functional  $\mathcal{F} : \mathcal{P}_2(\mathbb{R}^d) \rightarrow \mathbb{R}$ , the Wasserstein gradient flow [28, 29, 30]  $(q_t)_{t \geq 0} \subset \mathcal{P}_2(\mathbb{R}^d)$  represents the path of steepest descent for  $\mathcal{F}$  with respect to the Riemannian geometry of  $W_2$ . It is governed by the following continuity equation:

$$\partial_t q_t(\mathbf{x}_t) = -\text{grad}_{W_2} \mathcal{F}[q_t] = -\nabla_{\mathbf{x}} \cdot (q_t(\mathbf{x}_t) \mathbf{v}_t(\mathbf{x}_t)).$$

driven by the velocity field  $\mathbf{v}_t(\mathbf{x}_t) = -\nabla_{\mathcal{W}} \mathcal{F}[q_t](\mathbf{x}_t)$ . Both  $\text{grad}_{W_2} \mathcal{F}$  and  $\nabla_{\mathcal{W}} \mathcal{F}$  are commonly referred to as the *Wasserstein gradient* in the literature. Under appropriate regularity conditions, the latter admits the representation  $\nabla_{\mathcal{W}} \mathcal{F}[q_t](\mathbf{x}_t) = \nabla_{\mathbf{x}} \frac{\delta \mathcal{F}}{\delta q_t}(\mathbf{x}_t)$ . To illustrate, consider  $\mathcal{F}[q_t] = D_{\text{KL}}(q_t \| p)$ , the first variation yields  $\frac{\delta \mathcal{F}}{\delta q_t} = \log \frac{q_t}{p} + 1$  (See Appendix A.1). This gives the Wasserstein gradient as  $\nabla_{\mathbf{x}} \frac{\delta \mathcal{F}}{\delta q_t}(\mathbf{x}_t) = \nabla_{\mathbf{x}} \log q_t(\mathbf{x}_t) - \nabla_{\mathbf{x}} \log p(\mathbf{x}_t)$ , and the resulting particle dynamics:

$$\frac{d\mathbf{x}_t}{dt} = \mathbf{v}_t(\mathbf{x}_t) = -\nabla_{\mathbf{x}} \frac{\delta \mathcal{F}[q_t]}{\delta q_t}(\mathbf{x}_t) = \nabla_{\mathbf{x}} \log p(\mathbf{x}_t) - \nabla_{\mathbf{x}} \log q_t(\mathbf{x}_t).$$

precisely matches the PF-ODE associated with the overdamped Langevin SDE targeting the distribution  $p$  [31].

**Classifier-Free Guidance.** Classifier-Free Guidance (CFG) [32] controls conditioning strength without requiring a separate classifier. During training, the conditioning signal  $c$  (e.g., a text prompt) is randomly dropped, allowing the network to learn both a conditional predictor  $\epsilon_\phi(\mathbf{x}_t, t, c)$  and an

unconditional predictor  $\epsilon_\phi(\mathbf{x}_t, t, \emptyset)$ . At inference, these predictions are linearly extrapolated to form the guided noise estimate:

$$\hat{\epsilon}_\phi(\mathbf{x}_t, t, c) = \epsilon_\phi(\mathbf{x}_t, t, \emptyset) + \gamma(\epsilon_\phi(\mathbf{x}_t, t, c) - \epsilon_\phi(\mathbf{x}_t, t, \emptyset)),$$

where the guidance scale  $\gamma$  determines the conditioning strength. While  $\gamma = 1$  recovers the standard conditional model,  $\gamma > 1$  amplifies alignment with the condition  $c$ , typically at the expense of sample diversity. CFG remains the standard conditioning mechanism in modern text-to-image architectures.

### 3 Distilling 2D into 3D

**Score Distillation Sampling.** Score Distillation Sampling (SDS) [6, 33] leverages a pretrained 2D diffusion model as a prior to optimize a parameterized 3D representation  $\theta$ . At each optimization step, a timestep  $t$  and camera pose  $c$  are sampled, an image  $\mathbf{x}_0$  is rendered, and Gaussian noise  $\epsilon$  is added to obtain a noisy sample  $\mathbf{x}_t$ . The SDS gradient is computed as

$$\nabla_\theta \mathcal{L}_{\text{SDS}} = \mathbb{E}_{t, \epsilon, c} \left[ w(t) (\epsilon_\phi(\mathbf{x}_t, t, c) - \epsilon) \frac{\partial \mathbf{x}_0}{\partial \theta} \right],$$

where the noise-prediction network is treated with a stop-gradient operation during optimization. While SDS has enabled text-to-3D generation by distilling 2D Diffusion models, it typically relies on large CFG scales, often resulting in over-smoothed geometry and over-saturated textures. To mitigate these artifacts, Magic3D [13] introduces a coarse-to-fine pipeline that refines a low-resolution NeRF into a high-resolution mesh. Fantasia3D [14] improves fidelity by disentangling geometry and appearance via hybrid representations, while HiFA [34] adopts a suite of improvements—including square-root timestep annealing, image-space SDS, a  $z$ -variance loss, coarse-to-fine NeRF sampling, and kernel smoothing—to improve stability and generation quality.

**Score Distillation via Inversion.** Score Distillation with Inversion (SDI) [19] and the closely related Interval Score Matching (ISM) [35], modifies the SDS formulation by replacing stochastic noise perturbations with a deterministic DDIM inversion trajectory. Specifically, instead of sampling  $\epsilon$ , SDI computes a deterministic inversion noise  $\epsilon_{\text{inv}}$  from the current rendering, effectively reducing variance in the gradient estimate. This yields sharper results with enhanced texture detail compared to standard SDS.

**Variational Score Distillation.** ProlificDreamer [17] formulates text-to-3D generation within the framework of particle variational inference via Variational Score Distillation (VSD). In this approach, the gradient is defined as the difference between the noise prediction of the base diffusion model and that of a model adapted to the distribution of current renderings. This induces a Wasserstein gradient flow over the particle distribution, encouraging alignment with the target diffusion prior. However, VSD requires additional model adaptation, resulting in increased computational and memory overhead.

**3D-Aware Priors and the Janus Problem.** A separate line of work addresses the Janus problem, a multi-view inconsistency arising from ambiguous 2D supervision. Methods such as Zero-1-to-3 [36], SyncDreamer [37], Wonder3D [38], and MVDream [39] improve cross-view consistency through view-conditioned generation, often leveraging models adapted or trained using 3D-aware data. These approaches are orthogonal to our work, which instead focuses on improving the underlying distillation objective. In practice, we incorporate Perp-Neg [40] as a simple mitigation for Janus artifacts.

### 4 Motivating PFD from SDI

In this section, we develop the geometric intuition leading to PFD by first examining SDS and SDI, before presenting the formal PFD algorithm in the subsequent section. To simplify the exposition, we assume the identity rendering map,  $\frac{\partial \mathbf{x}_0}{\partial \theta} = I$ , i.e., the images themselves serve as parameters to be optimized. We adopt the particle variational inference perspective [41, 42, 43] and treat images as particles. Let  $q_0^\tau$  denote the empirical particle distribution at optimization iteration  $\tau$ . At each iteration, a particle  $\mathbf{x}_0 \sim q_0^\tau$  is sampled, its gradient is evaluated, and the particle is updated accordingly. We begin with the following observation.

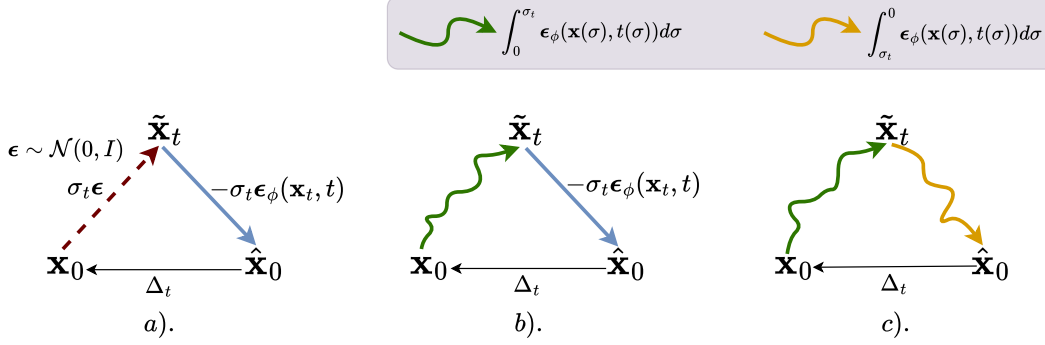


Figure 2: Comparison of different distillation gradients. (a) **SDS**: A noisy sample  $\tilde{\mathbf{x}}_t$  is obtained via Gaussian perturbation of  $\mathbf{x}_0$ , and the reverse mapping is approximated using a single-step estimate (posterior mean). (b) **SDI**: The forward mapping from  $\mathbf{x}_0$  to  $\tilde{\mathbf{x}}_t$  is computed by deterministic integration of the PF-ODE, whereas the reverse mapping remains a single-step approximation. (c) **PFD (Ours)**: Both forward and reverse trajectories are computed via integration of the PF-ODE, eliminating the posterior mean approximation.

**Claim.** *The DDIM posterior mean estimate of the clean sample  $\mathbf{x}_0$  conditioned on a noisy observation  $\mathbf{x}_t$ , given by*

$$\mathbb{E}[\mathbf{x}_0 \mid \mathbf{x}_t] = \frac{\mathbf{x}_t - \sqrt{1 - \alpha_t} \epsilon_\phi(\mathbf{x}_t, t)}{\sqrt{\alpha_t}} = \tilde{\mathbf{x}}_t - \sigma_t \epsilon_\phi(\mathbf{x}_t, t),$$

*admits an interpretation as a single explicit (forward Euler) discretization step of the DDIM PF-ODE evaluated at  $(\mathbf{x}_t, t)$ , integrating along the reverse-time trajectory from  $t$  to 0.*

*Proof.* Consider the DDIM-ODE from Section 2. Under a reparameterization in terms of the noise-to-signal level  $\sigma$ , the state trajectory  $\tilde{\mathbf{x}}(\sigma)$  evolves according to  $\frac{d\tilde{\mathbf{x}}(\sigma)}{d\sigma} = \epsilon_\phi(\mathbf{x}(\sigma), t(\sigma))$ . To estimate the clean sample  $\mathbf{x}_0$  (corresponding to  $\sigma = 0$ ) from the noisy state  $\tilde{\mathbf{x}}_t$  at  $\sigma_t$ , we approximate the integral using a single forward Euler step with step size  $\Delta\sigma = -\sigma_t$ :

$$\mathbf{x}_0 \approx \tilde{\mathbf{x}}_t + \Delta\sigma \left. \frac{d\tilde{\mathbf{x}}(\sigma)}{d\sigma} \right|_{\sigma=\sigma_t} = \tilde{\mathbf{x}}_t - \sigma_t \epsilon_\phi(\mathbf{x}_t, t).$$

This shows that the posterior mean is mathematically equivalent to a single Euler step along the reverse PF-ODE trajectory.  $\square$

#### 4.1 SDS Gradient.

In SDS, the gradient is given by the difference between the predicted noise  $\epsilon_\phi$  and the injected noise  $\epsilon$ . Using the  $\sigma$ -parameterization,

$$\epsilon = \frac{\tilde{\mathbf{x}}_t - \mathbf{x}_0}{\sigma_t}, \quad \epsilon_\phi = \frac{\tilde{\mathbf{x}}_t - \hat{\mathbf{x}}_0}{\sigma_t},$$

where  $\hat{\mathbf{x}}_0$  denotes the clean estimate obtained via the posterior mean. The resulting gradient is therefore proportional to the residual  $\Delta_t = \mathbf{x}_0 - \hat{\mathbf{x}}_0$ . Geometrically (Figure 2a),  $\mathbf{x}_0$  is mapped to  $\tilde{\mathbf{x}}_t$  by adding noise, and the reverse mapping to  $\hat{\mathbf{x}}_0$  corresponds to a single Euler step along the PF-ODE induced by the diffusion prior  $\{p_t\}_t$ . The gradient thus corresponds to the displacement vector from  $\hat{\mathbf{x}}_0$  to  $\mathbf{x}_0$ .

#### 4.2 SDI Gradient.

In SDI, the gradient remains proportional to the direction  $\mathbf{x}_0 - \hat{\mathbf{x}}_0$ , while the forward process is modified. Rather than obtaining  $\tilde{\mathbf{x}}_t$  through stochastic perturbation, SDI employs deterministic DDIM inversion to map  $\mathbf{x}_0$  to  $\tilde{\mathbf{x}}_t$ . The reverse mapping in SDI, however, still relies on a single step Euler approximation to recover  $\hat{\mathbf{x}}_0$  (Figure 2b).

**DDIM Inversion as PF-ODE Flow of  $\{q_t^\tau\}_t$ .** In practice, however, SDI does not explicitly model or adapt to the score  $\nabla_{\mathbf{x}} \log q_t^\tau(\mathbf{x})$ —where  $q_t^\tau$  denotes the forward noised distribution of the current particles—as would be done in VSD. Instead, it directly applies the standard DDIM inversion procedure, which can be retrospectively interpreted as integrating the PF-ODE associated with the marginals  $\{q_t^\tau\}_t$ , under the notion that the unconditioned diffusion model serves as a surrogate for the score of the particle distribution.

This approximation is implicit in several related formulations. In particular, CSD can be viewed as an approximation to VSD, where  $\epsilon_\phi(\mathbf{x}_t, t, \emptyset)$  substitutes for the score of the current particle distribution rather than the adapted prediction  $\epsilon_{\text{LoRA}}(\mathbf{x}_t, t, c)$ . In the text-to-3D setting, this approximation can be partially justified by the observation that rendered images typically remain close to the manifold of natural images, making the approximation  $\nabla_{\mathbf{x}} \log q_t^\tau(\mathbf{x}) \approx \nabla_{\mathbf{x}} \log p_t(\mathbf{x} \mid \emptyset)$  reasonable.

**Explanation of Negative CFG in SDI.** Under the above interpretation, the null-text-conditioned score used in the DDIM inversion may be viewed as the source prediction  $\epsilon_{\text{src}} = \epsilon_\phi(\mathbf{x}_t, t, \emptyset)$ , while the target-conditioned prediction is given by  $\epsilon_{\text{tgt}} = \epsilon_\phi(\mathbf{x}_t, t, c)$ . Thus, under standard CFG, the resulting noise prediction takes the form  $\epsilon_{\text{src}} + \gamma(\epsilon_{\text{tgt}} - \epsilon_{\text{src}})$ , which steers the trajectory toward the target distribution along the direction  $(\epsilon_{\text{tgt}} - \epsilon_{\text{src}})$ . Rewriting the expression gives,

$$\epsilon_{\text{src}} + \gamma(\epsilon_{\text{tgt}} - \epsilon_{\text{src}}) = \epsilon_{\text{tgt}} + (1 - \gamma)(\epsilon_{\text{src}} - \epsilon_{\text{tgt}}).$$

Consequently, exchanging the roles of source and target distributions is equivalent to replacing the guidance scale  $\gamma$  with  $1 - \gamma$ . Therefore, realizing the symmetric form

$$\epsilon_{\text{tgt}} + \gamma(\epsilon_{\text{src}} - \epsilon_{\text{tgt}})$$

with an effective guidance scale  $\gamma$  corresponds to a user-specified CFG guidance scale  $\gamma_{\text{cfg}} = 1 - \gamma$ . For  $\gamma > 1$ , this gives  $\gamma_{\text{cfg}} < 0$ , explaining the negative CFG scales employed in SDI.

This perspective naturally motivates our proposed extension (Figure 2c): replacing the single-step reverse approximation with numerical integration of the reverse-time PF-ODE trajectory. In the following section, we show that, under appropriate assumptions, this construction results in a well-defined sampling procedure.

## 5 Probability-Flow Distillation

Building on the analysis in the previous section, we formally introduce *Probability-Flow Distillation* as a general sampling-by-distillation framework. The objective is to optimize a distribution  $q_0 \in \mathcal{P}(\mathbb{R}^d)$ , represented empirically by a finite ensemble of particles  $\{\mathbf{x}_0^{(i)}\}_{i=1}^N$ , such that  $q_0$  converges toward the target distribution  $p_0$  learned by the diffusion model.

**PFD Algorithm.** The PFD algorithm is summarized in Appendix B. As in standard SDS-based methods, we first sample a time step  $t \sim \mathcal{U}(0, T)$ . We then simulate the forward PF-ODE associated with the marginals  $\{q_t^\tau\}_{t \in [0, T]}$ , mapping the particle from  $\mathbf{x}_0$  to an intermediate noisy state  $\mathbf{x}_t$ . From  $\mathbf{x}_t$ , we subsequently simulate the reverse PF-ODE corresponding to the target marginals  $\{p_t\}_{t \in [0, T]}$ , producing a predicted clean sample  $\hat{\mathbf{x}}_0$ . When implemented through automatic differentiation using a surrogate loss, both PF-ODEs are solved under a stop-gradient operation so that gradients are not backpropagated through the score evaluations along the trajectories. As established in Section 4, the discrepancy  $\Delta_t$  defines a stochastic gradient estimator whose expectation governs the evolution of the particles.

**Theoretical Characterization.** In Theorem 1, we establish that the PFD gradient  $\mathbb{E}_t[\Delta_t]$  coincides with the Wasserstein gradient of a time-averaged KL divergence functional between the marginals  $q_t^\tau$  and  $p_t$ . Consequently, the induced evolution of  $q_0^\tau$  follows a gradient flow in Wasserstein space. Moreover, the functional attains its global minimum at  $q_0^\tau = p_0$  (see Appendix C.4.1 of [17]), implying convergence of the particle ensemble toward the target distribution under the induced dynamics.

**Theorem 1** (PFD as Exact Wasserstein Gradient Flow). *Assume that both the forward and reverse PF-ODEs are governed by a linear drift term  $\mathbf{f}(\mathbf{x}, t) = a(t)\mathbf{x}$  and a scalar diffusion coefficient  $g(t)$ . Then, the gradient  $\mathbb{E}_t[\Delta_t]$  defined by PFD exactly matches the Wasserstein gradient of a weighted time-averaged KL divergence functional  $\mathcal{F}[q_0]$ :*

$$\mathbb{E}_t[\Delta_t] = \nabla_{\mathbf{x}} \left( \frac{\delta \mathcal{F}[q_0]}{\delta q_0(\mathbf{x})} \right) (\mathbf{x}_0),$$

where the functional is given by  $\mathcal{F}[q_0] = \mathbb{E}_t[w(t)D_{\text{KL}}(q_t||p_t)]$ . Here,  $q_t$  denotes the marginal distribution of  $q_0$  perturbed to time  $t$ ,  $\{p_t\}_{t \in [0,1]}$  represents the target diffusion prior, and the weighting function is given by  $w(t) = \frac{1}{2}(T-t)g(t)^2c(t,0)^2$  with the scaling factor  $c(t,0) = \exp\left(-\int_0^t a(s)ds\right)$ .

*Proof.* See Appendix A. □

**Empirical Evaluation.** To empirically validate the proposed method, we conduct a 2D experiment comparing SDS, SDI, and PFD on a toy dataset consisting of concentric circles in  $\mathbb{R}^2$ . In this setting, a primary noise-prediction network is pre-trained to model the score of the target diffusion prior  $\{p_t\}_{t \in [0,T]}$ . To simulate the forward PF-ODE required by SDI and PFD, a secondary network is trained at each optimization step to estimate the score of the current empirical marginals  $\{q_t^\tau\}_{t \in [0,T]}$ . We adopt the Variance Exploding (VE) SDE formulation for simplicity. Since both VE-SDE and VP-SDE are characterized by linear drift and time-dependent diffusion coefficients, the assumptions of Theorem 1 hold exactly in this setting, as well as in the 3D generation experiments presented in the subsequent section.

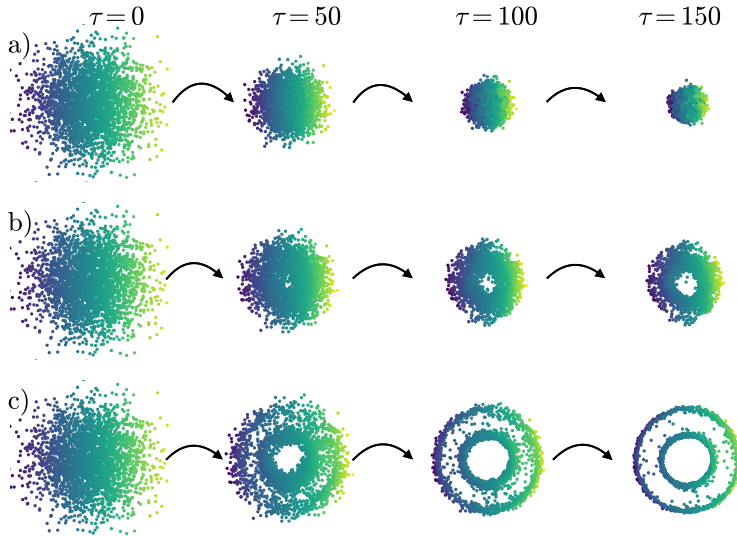


Figure 3: Visualization of 2D particle evolution targeting a concentric circles dataset. The rows depict the empirical distributions across successive optimization steps ( $\tau$ ) for (a) SDS, (b) SDI, and (c) PFD (Ours).

**Discussion.** Figure 3 illustrates the evolution of the particle ensemble across optimization steps  $\tau$ . SDS rapidly collapses to a single mode, reflecting its tendency to optimize a point estimate rather than perform sampling. SDI partially alleviates this issue but still fails to capture the full support of the target distribution. In contrast, PFD successfully recovers the complete multi-modal structure. This geometric behavior in the 2D setting mirrors empirical observations in high-dimensional generative tasks: SDS often produces over-smoothed textures due to its mode-seeking nature; SDI provides partial improvements but the resulting 3D models still lack fine-grained details; in contrast, PFD, as a distribution-matching algorithm, preserves fine details (See Appendix G).

## 6 Text-to-3D Generation with PFD

### 6.1 Implementation and Evaluation

**Practical Approximations.** We adapt PFD to the setting of text-to-3D generation using the approximation discussed in Section 4.2. Specifically, rather than modeling the evolving particle distribution  $q_0^\tau$  and learning its corresponding score function, we employ standard DDIM inversion. This eliminates the need to maintain a particle ensemble, allowing optimization to be performed in the single-particle regime ( $N = 1$ ). In practice, explicitly representing and evolving multiple particles together with their induced distribution would incur substantial computational overhead. Despite these approximations, PFD produces 3D assets with improved textural detail compared to prior approaches. An overview of the complete pipeline is shown in Figure 4. A comprehensive description of the implementation details of both our method and the evaluated baselines, along with the licenses of the models and tools employed, is provided in Appendix D.

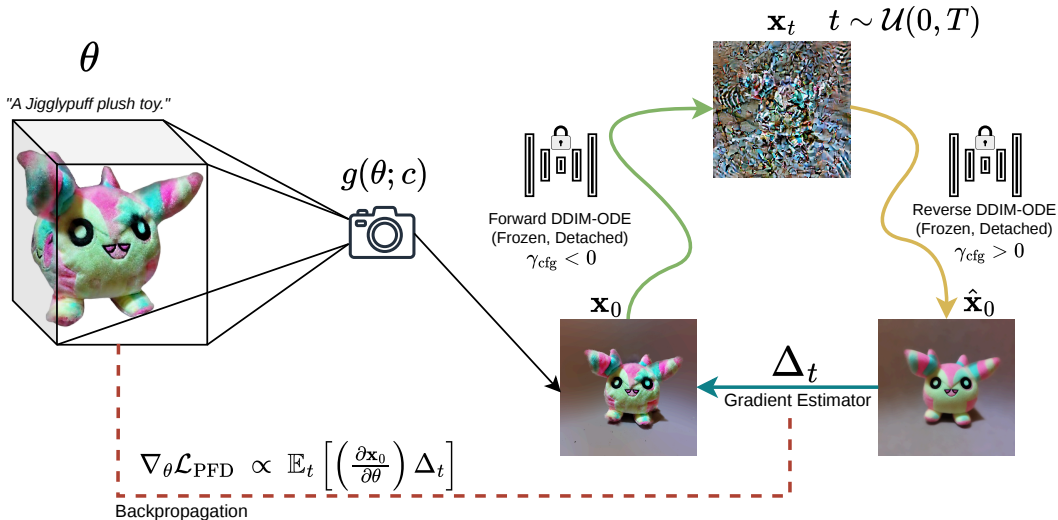


Figure 4: Illustration of the proposed text-to-3D generation pipeline based on PFD. The DDIM-ODE is solved in both forward and reverse directions to compute the distillation gradient.

**Comparison.** We compare PFD with SDS, SDI, VSD, and CSD. SDS serves as the foundational baseline, SDI as the most closely related method upon which our approach builds, and VSD as a related distribution-matching framework, with CSD representing an approximation to VSD analogous to the approximation employed in our 3D instantiation of PFD. Qualitative comparisons are shown in Figure 5, with additional results provided in Appendix G. Quantitatively, we report CLIP score [44] and CLIP-IQA [45] metrics, including quality (“Good photo” vs. “Bad photo”), sharpness (“Sharp photo” vs. “Blurry photo”), and naturalness (“Natural photo” vs. “Synthetic photo”), computed using the ViT-B/32 backbone and torchmetrics [46], together with ImageReward (IR) [47]. We additionally report VRAM usage and wall-clock runtime. All quantitative results are summarized in Table 1.

Notably, PFD achieves higher ImageReward scores than competing approaches, indicating stronger alignment with learned human preferences. Furthermore, PFD exhibits VRAM usage comparable to SDI, since gradients are not propagated through the diffusion model and its activations therefore do not need to be retained for backpropagation, thus the increased number of sequential U-Net evaluations to primarily affect runtime rather than memory usage.

### 6.2 Ablation Study

We provide a study of some components in our implementation in Appendix E. The proposed extension (Appendix E.1) produces richer textures and finer detail compared to SDI, with the improvements becoming more evident at higher resolutions. The CFG scale (Appendix E.2) strongly



Figure 5: Qualitative comparison of 3D objects generated by SDS, SDI, VSD, CSD, and PFD.

Table 1: Quantitative comparison of SDS, SDI, VSD, CSD, and PFD on 3D object generation. Results are averaged over 20 generated examples per method.

Method	CLIP $\uparrow$	CLIP-IQA $\uparrow$			IR $\uparrow$	VRAM $\downarrow$	Time $\downarrow$
		Quality	Sharpness	Naturalness			
SDS (10k)	30.52	0.26	0.05	0.20	-0.82	~ 9 GB	~ 45 mins
SDI (10k)	31.29	0.28	0.16	0.27	-0.13	~ 34 GB	~ 120 mins
VSD (10k)	32.66	0.58	0.30	0.36	0.38	~ 45 GB	~ 120 mins
CSD (20k)	32.24	0.49	0.23	0.28	0.18	~ 9 GB	~ 120 mins
<b>PFD (Ours) (7.5k)</b>	<b>32.89</b>	<b>0.57</b>	<b>0.21</b>	<b>0.28</b>	<b>0.54</b>	<b>~ 36 GB</b>	<b>~ 120 mins</b>

influences optimization stability, where excessively large magnitudes degrade generation quality, and the correct sign convention is essential. Time annealing (Appendix E.3) further improves fine-scale detail and color quality by focusing optimization on lower-noise regimes during later stages.

## 7 Conclusion

We introduced *Probability-Flow Distillation* (PFD), a theoretically grounded distillation method for sampling rooted in Wasserstein gradient flows that extends prior work through principled insights, and applied it to text-to-3D generation.

**Limitations and Future Work.** Despite producing competitive results, PFD retains limitations shared with prior distillation-based methods. In particular, it remains susceptible to the Janus problem (See Appendix F), as well as artifacts such as floaters and unintended scene expansion. Incorporating stronger geometric priors and multi-view consistency constraints may improve structural fidelity. Additionally, sequential U-Net evaluations introduce significant computational overhead. Future work may explore more efficient PF-ODE solvers and trajectory distillation methods that approximate PF-ODE solutions in a few steps. Another promising direction is to extend PFD for 3D generation beyond the single-particle setting while reducing the associated computational cost.

**Broader Impact.** Advances in text-to-3D generation may enable applications in content creation, virtual environments, and design, while also raising concerns about synthetic or misleading media. Accordingly, careful deployment and appropriate safeguards remain important when applying such systems in practice. Since PFD extends existing distillation-based text-to-3D methods rather than introducing a fundamentally new generation capability, it does not substantially alter the associated risk profile.

## References

- [1] Jonathan Ho, Ajay Jain, and Pieter Abbeel. Denoising diffusion probabilistic models. In *Advances in Neural Information Processing Systems*, volume 33, pages 6840–6851, 2020.
- [2] Robin Rombach, Andreas Blattmann, Dominik Lorenz, Patrick Esser, and Björn Ommer. High-resolution image synthesis with latent diffusion models. *CoRR*, abs/2112.10752, 2021. URL <https://arxiv.org/abs/2112.10752>.
- [3] Chitwan Saharia, William Chan, Saurabh Saxena, Lala Li, Jay Whang, Emily Denton, Seyed Kamyar Seyed Ghasemipour, Raphael Gontijo-Lopes, Burcu Karagol Ayan, Tim Salimans, Jonathan Ho, David J. Fleet, and Mohammad Norouzi. Photorealistic text-to-image diffusion models with deep language understanding. In Alice H. Oh, Alekh Agarwal, Danielle Belgrave, and Kyunghyun Cho, editors, *Advances in Neural Information Processing Systems*, 2022. URL <https://openreview.net/forum?id=08Yk-n512A1>.
- [4] Tero Karras, Miika Aittala, Timo Aila, and Samuli Laine. Elucidating the design space of diffusion-based generative models. In Alice H. Oh, Alekh Agarwal, Danielle Belgrave, and Kyunghyun Cho, editors, *Advances in Neural Information Processing Systems*, 2022. URL <https://openreview.net/forum?id=k7FuTOWM0c7>.
- [5] Yaron Lipman, Ricky T. Q. Chen, Heli Ben-Hamu, Maximilian Nickel, and Matthew Le. Flow matching for generative modeling. In *The Eleventh International Conference on Learning Representations*, 2023. URL <https://openreview.net/forum?id=PqvMRDCJT9t>.
- [6] Ben Poole, Ajay Jain, Jonathan T. Barron, and Ben Mildenhall. Dreamfusion: Text-to-3d using 2d diffusion. *arXiv*, 2022.
- [7] Ben Mildenhall, Pratul P. Srinivasan, Matthew Tancik, Jonathan T. Barron, Ravi Ramamoorthi, and Ren Ng. Nerf: Representing scenes as neural radiance fields for view synthesis. In *ECCV*, 2020.
- [8] Thomas Müller, Alex Evans, Christoph Schied, and Alexander Keller. Instant neural graphics primitives with a multiresolution hash encoding. *ACM Trans. Graph.*, 41(4):102:1–102:15, July 2022. doi: 10.1145/3528223.3530127. URL <https://doi.org/10.1145/3528223.3530127>.
- [9] Tianchang Shen, Jun Gao, Kangxue Yin, Ming-Yu Liu, and Sanja Fidler. Deep marching tetrahedra: a hybrid representation for high-resolution 3d shape synthesis. In *Advances in Neural Information Processing Systems (NeurIPS)*, 2021.
- [10] Bernhard Kerbl, Georgios Kopanas, Thomas Leimkühler, and George Drettakis. 3d gaussian splatting for real-time radiance field rendering. *ACM Transactions on Graphics*, 42(4), July 2023. URL <https://repo-sam.inria.fr/fungraph/3d-gaussian-splatting/>.
- [11] Amir Hertz, Kfir Aberman, and Daniel Cohen-Or. Delta denoising score. In *2023 IEEE/CVF International Conference on Computer Vision (ICCV)*, pages 2328–2337, 2023. doi: 10.1109/ICCV51070.2023.00221.
- [12] Oren Katzir, Or Patashnik, Daniel Cohen-Or, and Dani Lischinski. Noise-free score distillation. In *The Twelfth International Conference on Learning Representations*, 2024. URL <https://openreview.net/forum?id=d1IMcmlAdk>.
- [13] Chen-Hsuan Lin, Jun Gao, Luming Tang, Towaki Takikawa, Xiaohui Zeng, Xun Huang, Karsten Kreis, Sanja Fidler, Ming-Yu Liu, and Tsung-Yi Lin. Magic3d: High-resolution text-to-3d content creation. In *Proceedings of the IEEE/CVF Conference on Computer Vision and Pattern Recognition (CVPR)*, pages 300–309, 2023.
- [14] Rui Chen, Yongwei Chen, Ningxin Jiao, and Kui Jia. Fantasia3d: Disentangling geometry and appearance for high-quality text-to-3d content creation. In *Proceedings of the IEEE/CVF International Conference on Computer Vision (ICCV)*, pages 22246–22256, October 2023.
- [15] Taoran Yi, Jiemin Fang, Junjie Wang, Guanjun Wu, Lingxi Xie, Xiaopeng Zhang, Wenyu Liu, Qi Tian, and Xinggang Wang. Gaussiandreamer: Fast generation from text to 3d gaussians by bridging 2d and 3d diffusion models. In *CVPR*, 2024.
- [16] Xin Yu, Yuan-Chen Guo, Yangguang Li, Ding Liang, Song-Hai Zhang, and XIAOJUAN QI. Text-to-3d with classifier score distillation. In *The Twelfth International Conference on Learning Representations*, 2024. URL <https://openreview.net/forum?id=ktG8Tun1Cy>.

- [17] Zhengyi Wang, Cheng Lu, Yikai Wang, Fan Bao, Chongxuan Li, Hang Su, and Jun Zhu. Prolificdreamer: High-fidelity and diverse text-to-3d generation with variational score distillation. In *Advances in Neural Information Processing Systems (NeurIPS)*, 2023.
- [18] Edward J Hu, yelong shen, Phillip Wallis, Zeyuan Allen-Zhu, Yuanzhi Li, Shean Wang, Lu Wang, and Weizhu Chen. LoRA: Low-rank adaptation of large language models. In *International Conference on Learning Representations*, 2022. URL <https://openreview.net/forum?id=nZeVKeeFYf9>.
- [19] Artem Lukoianov, Haitz S’aez de Oc’ariz Borde, Kristjan Greenewald, Vitor Guizilini, Timur Bagautdinov, Vincent Sitzmann, and Justin M Solomon. Score distillation via reparametrized ddim. *Advances in Neural Information Processing Systems*, 37:26011–26044, 2024.
- [20] David McAllister, Songwei Ge, Jia-Bin Huang, David W. Jacobs, Alexei A. Efros, Aleksander Holynski, and Angjoo Kanazawa. Rethinking score distillation as a bridge between image distributions. In *Advances in Neural Information Processing Systems*, 2024.
- [21] Xuan Su, Jiaming Song, Chenlin Meng, and Stefano Ermon. Dual diffusion implicit bridges for image-to-image translation. In *The Eleventh International Conference on Learning Representations*, 2023. URL <https://openreview.net/forum?id=5HLoTvVGDe>.
- [22] Brian D.O. Anderson. Reverse-time diffusion equation models. *Stochastic Processes and their Applications*, 12(3):313–326, 1982. ISSN 0304-4149. doi: [https://doi.org/10.1016/0304-4149\(82\)90051-5](https://doi.org/10.1016/0304-4149(82)90051-5). URL <https://www.sciencedirect.com/science/article/pii/0304414982900515>.
- [23] Pascal Vincent. A connection between score matching and denoising autoencoders. *Neural Computation*, 23(7):1661–1674, 2011. doi: 10.1162/NECO\_a\_00142.
- [24] Yang Song, Jascha Sohl-Dickstein, Diederik P Kingma, Abhishek Kumar, Stefano Ermon, and Ben Poole. Score-based generative modeling through stochastic differential equations. In *International Conference on Learning Representations*, 2021. URL <https://openreview.net/forum?id=PXTIG12RRHS>.
- [25] Jiaming Song, Chenlin Meng, and Stefano Ermon. Denoising diffusion implicit models. In *International Conference on Learning Representations*, 2021. URL <https://openreview.net/forum?id=St1giarCHLP>.
- [26] Prafulla Dhariwal and Alexander Quinn Nichol. Diffusion models beat GANs on image synthesis. In A. Beygelzimer, Y. Dauphin, P. Liang, and J. Wortman Vaughan, editors, *Advances in Neural Information Processing Systems*, 2021. URL <https://openreview.net/forum?id=AAWuCVzaVt>.
- [27] Ron Mokady, Amir Hertz, Kfir Aberman, Yael Pritch, and Daniel Cohen-Or. Null-text inversion for editing real images using guided diffusion models. In *2023 IEEE/CVF Conference on Computer Vision and Pattern Recognition (CVPR)*, pages 6038–6047, 2023. doi: 10.1109/CVPR52729.2023.00585.
- [28] Cédric Villani. *Topics in Optimal Transportation*, volume 58 of *Graduate Studies in Mathematics*. American Mathematical Society, Providence, RI, 2003.
- [29] Alessio Figalli. An introduction to optimal transport and wasserstein gradient flows, 2023. URL <https://people.math.ethz.ch/~afigalli/lecture-notes-pdf/An-introduction-to-optimal-transport-and-Wasserstein-gradient-flows.pdf>. Lecture notes from the School “Optimal Transport on Quantum Structures”, Erdős Center, Alfréd Rényi Institute of Mathematics, September 19–23, 2022.
- [30] Luigi Ambrosio, Nicola Gigli, and Giuseppe Savaré. *Gradient Flows in Metric Spaces and in the Space of Probability Measures*. Birkhäuser, 2008.
- [31] Wikipedia contributors. Langevin dynamics — Wikipedia, the free encyclopedia. [https://en.wikipedia.org/w/index.php?title=Langevin\\_dynamics&oldid=1348039185](https://en.wikipedia.org/w/index.php?title=Langevin_dynamics&oldid=1348039185).
- [32] Jonathan Ho and Tim Salimans. Classifier-free diffusion guidance. In *NeurIPS 2021 Workshop on Deep Generative Models and Downstream Applications*, 2021. URL <https://openreview.net/forum?id=qw8AKxfYbI>.
- [33] Haochen Wang, Xiaodan Du, Jiahao Li, Raymond A. Yeh, and Greg Shakhnarovich. Score jacobian chaining: Lifting pretrained 2d diffusion models for 3d generation. In *Proceedings*

- of the *IEEE/CVF Conference on Computer Vision and Pattern Recognition (CVPR)*, pages 7047–7056, 2023.
- [34] Junzhe Zhu, Peiye Zhuang, and Sanmi Koyejo. HIFA: High-fidelity text-to-3d generation with advanced diffusion guidance. In *The Twelfth International Conference on Learning Representations*, 2024. URL <https://openreview.net/forum?id=IZMPWmcS3H>.
- [35] Yixun Liang, Xin Yang, Jiantao Lin, Haodong Li, Xiaogang Xu, and Yingcong Chen. Lucid-dreamer: Towards high-fidelity text-to-3d generation via interval score matching. In *Proceedings of the IEEE/CVF Conference on Computer Vision and Pattern Recognition (CVPR)*, pages 6517–6526, June 2024.
- [36] Ruoshi Liu, Rundi Wu, Basile Van Hoorick, Pavel Tokmakov, Sergey Zakharov, and Carl Vondrick. Zero-1-to-3: Zero-shot one image to 3d object. In *Proceedings of the IEEE/CVF International Conference on Computer Vision (ICCV)*, pages 9298–9309, October 2023.
- [37] Yuan Liu, Cheng Lin, Zijiao Zeng, Xiaoxiao Long, Lingjie Liu, Taku Komura, and Wenping Wang. Syncdreamer: Generating multiview-consistent images from a single-view image. In *The Twelfth International Conference on Learning Representations*, 2024. URL <https://openreview.net/forum?id=MN3yH2ovHb>.
- [38] Xiaoxiao Long, Yuan-Chen Guo, Cheng Lin, Yuan Liu, Zhiyang Dou, Lingjie Liu, Yuexin Ma, Song-Hai Zhang, Marc Habermann, Christian Theobalt, and Wenping Wang. Wonder3d: Single image to 3d using cross-domain diffusion. In *Proceedings of the IEEE/CVF Conference on Computer Vision and Pattern Recognition (CVPR)*, 2024. doi: 10.1109/CVPR52733.2024.00951.
- [39] Yichun Shi, Peng Wang, Jianglong Ye, Long Mai, Kejie Li, and Xiao Yang. MVDream: Multi-view diffusion for 3d generation. In *The Twelfth International Conference on Learning Representations*, 2024. URL <https://openreview.net/forum?id=FUgrjq2pbB>.
- [40] Mohammadreza Armandpour, Huangjie Zheng, Ali Sadeghian, Amir Sadeghian, and Mingyuan Zhou. Re-imagine the negative prompt algorithm: Transform 2d diffusion into 3d, alleviate janus problem and beyond. *arXiv preprint arXiv:2304.04968*, 2023.
- [41] Qiang Liu and Dilin Wang. Stein variational gradient descent: A general purpose bayesian inference algorithm. In *Advances in Neural Information Processing Systems 29 (NeurIPS 2016)*, 2016.
- [42] Chang Liu and Jun Zhu. Chapter 10 - geometry in sampling methods: A review on manifold mcmc and particle-based variational inference methods. In Arni S.R. Srinivasa Rao, G. Alastair Young, and C.R. Rao, editors, *Advancements in Bayesian Methods and Implementation*, volume 47 of *Handbook of Statistics*, pages 239–293. Elsevier, 2022. doi: <https://doi.org/10.1016/bs.host.2022.07.004>. URL <https://www.sciencedirect.com/science/article/pii/S0169716122000426>.
- [43] Changyou Chen, Ruiyi Zhang, Wenlin Wang, Bai Li, and Liqun Chen. A unified particle-optimization framework for scalable bayesian sampling. In *Conference on Uncertainty in Artificial Intelligence*, 2018. URL <https://api.semanticscholar.org/CorpusID:44111731>.
- [44] Jack Hessel, Ari Holtzman, Maxwell Forbes, Ronan Le Bras, and Yejin Choi. CLIPScore: A reference-free evaluation metric for image captioning. In Marie-Francine Moens, Xuanjing Huang, Lucia Specia, and Scott Wen-tau Yih, editors, *Proceedings of the 2021 Conference on Empirical Methods in Natural Language Processing*, pages 7514–7528, Online and Punta Cana, Dominican Republic, November 2021. Association for Computational Linguistics. doi: 10.18653/v1/2021.emnlp-main.595. URL <https://aclanthology.org/2021.emnlp-main.595/>.
- [45] Jianyi Wang, Kelvin CK Chan, and Chen Change Loy. Exploring clip for assessing the look and feel of images. In *AAAI*, 2023.
- [46] Nicki Skafte Detlefsen, Jiri Borovec, Justus Schock, Ananya Harsh Jha, Teddy Koker, Luca Di Liello, Daniel Stancl, Changsheng Quan, Maxim Grechkin, and William Falcon. Torchmetrics - measuring reproducibility in pytorch. *Journal of Open Source Software*, 7(70):4101, 2022. doi: 10.21105/joss.04101. URL <https://doi.org/10.21105/joss.04101>.
- [47] Jiazheng Xu, Xiao Liu, Yuchen Wu, Yuxuan Tong, Qinkai Li, Ming Ding, Jie Tang, and Yuxiao Dong. Imagereward: learning and evaluating human preferences for text-to-image generation.

- In *Proceedings of the 37th International Conference on Neural Information Processing Systems*, pages 15903–15935, 2023.
- [48] W. Greiner and J. Reinhardt. *Field Quantization*. Springer, 1996. ISBN 9783540591795. URL <https://books.google.co.in/books?id=VvBAvf0wSrIC>.
- [49] E. Engel and R.M. Dreizler. *Density Functional Theory: An Advanced Course*. Theoretical and Mathematical Physics. Springer Berlin Heidelberg, 2011. ISBN 9783642140891. URL <https://books.google.co.in/books?id=o9byjwEACAAJ>.
- [50] Philip Hartman. *Ordinary Differential Equations*. Society for Industrial and Applied Mathematics, second edition, 2002. doi: 10.1137/1.9780898719222. URL <https://epubs.siam.org/doi/abs/10.1137/1.9780898719222>.
- [51] Yuan-Chen Guo, Ying-Tian Liu, Ruizhi Shao, Christian Laforte, Vikram Voleti, Guan Luo, Chia-Hao Chen, Zi-Xin Zou, Chen Wang, Yan-Pei Cao, and Song-Hai Zhang. threestudio: A unified framework for 3d content generation. <https://github.com/threestudio-project/threestudio>, 2023.
- [52] Cheng Lu, Yuhao Zhou, Fan Bao, Jianfei Chen, Chongxuan Li, and Jun Zhu. DPM-solver++: Fast solver for guided sampling of diffusion probabilistic models, 2023. URL <https://openreview.net/forum?id=4vGwQqvuid5>.
- [53] StabilityAI. DeepFloyd IF. <https://github.com/deep-floyd/IF>, 2023.
- [54] Patrick von Platen, Suraj Patil, Anton Lozhkov, Pedro Cuenca, Nathan Lambert, Kashif Rasul, Mishig Davaadorj, Dhruv Nair, Sayak Paul, William Berman, Yiyi Xu, Steven Liu, and Thomas Wolf. Diffusers: State-of-the-art diffusion models. <https://github.com/huggingface/diffusers>, 2022.

## A Proof of Theorem 1

**Assumption and Definitions.** We assume that the underlying diffusion process is governed by an Itô SDE featuring a linear drift term,  $\mathbf{f}(\mathbf{x}, t) = a(t)\mathbf{x}$  with a scalar diffusion coefficient  $g(t)$  (e.g., VP-SDE). Let  $T_{\#}\mu$  denote the pushforward of a probability measure  $\mu$  under a generic map  $T$ . For a PF-ODE, we define the flow map  $\Phi(t, s, \cdot) : \mathbb{R}^d \rightarrow \mathbb{R}^d$  as the transformation from a state at time  $s$  to time  $t$  and denote its spatial Jacobian by  $D_{\mathbf{x}}\Phi(t, s, \cdot)$ , suppressing time arguments when clear from context. We consider the interaction between two distinct families of distributions, the target marginals  $\{p_t\}_{t \in [0, T]}$  with the associated PF-ODE flow map  $\Phi_p(t, s, \cdot)$ , and the generated particle distribution  $q_0$  together with its forward marginals  $\{q_t\}_{t \in [0, T]}$ . The forward noising process admits an equivalent deterministic PF-ODE representation with flow map  $\Phi_q(t, s, \cdot)$ , which produces the pushforward relation  $q_t = (\Phi_q(t, 0, \cdot))_{\#}q_0$ .

The proof proceeds in two parts. In Section A.1, we derive a simplified expression for the Wasserstein gradient. In Section A.2, we then show that the PFD gradient coincides with this expression.

### A.1 Derivation of the Wasserstein Gradient

To compute the Wasserstein gradient,  $\nabla_{\mathbf{x}_0} \frac{\delta \mathcal{F}[q_0]}{\delta q_0(\mathbf{x}_0)}$ , we first establish a few useful results. Lemmas 1 and 2 are standard, while we derive Lemmas 3 and 4 specific to the formulation.

**Lemma 1.** *For any  $p, q \in \mathcal{P}_2(\mathbb{R}^d)$ , the first variation of the Kullback–Leibler divergence  $D_{\text{KL}}[q] = D_{\text{KL}}(q||p)$  with respect to the density  $q$  is:*

$$\frac{\delta D_{\text{KL}}[q]}{\delta q(\mathbf{x})} = \log \left( \frac{q(\mathbf{x})}{p(\mathbf{x})} \right) + 1.$$

*Proof.* Though this is a standard identity in variational calculus, we include the proof here for completeness. Let  $q_{\varepsilon}(\mathbf{x}) = q(\mathbf{x}) + \varepsilon\eta(\mathbf{x})$  be a valid density perturbation, where the test function satisfies  $\int \eta(\mathbf{x}) d\mathbf{x} = 0$  to strictly conserve the probability mass. The first-order variation is:

$$\left. \frac{d}{d\varepsilon} D_{\text{KL}}[q_{\varepsilon}] \right|_{\varepsilon=0} = \int \left. \frac{d}{d\varepsilon} \left[ (q(\mathbf{x}) + \varepsilon\eta(\mathbf{x})) \log \frac{q(\mathbf{x}) + \varepsilon\eta(\mathbf{x})}{p(\mathbf{x})} \right] \right|_{\varepsilon=0} d\mathbf{x}.$$

Applying the product rule yields:

$$\int \left[ \eta(\mathbf{x}) \log \frac{q(\mathbf{x})}{p(\mathbf{x})} + q(\mathbf{x}) \left( \frac{p(\mathbf{x})}{q(\mathbf{x})} \right) \left( \frac{\eta(\mathbf{x})}{p(\mathbf{x})} \right) \right] d\mathbf{x} = \int \eta(\mathbf{x}) \left( \log \frac{q(\mathbf{x})}{p(\mathbf{x})} + 1 \right) d\mathbf{x}.$$

By the standard definition of the functional derivative [48],  $\frac{d}{d\varepsilon} \mathcal{F}[q_\varepsilon] \Big|_{\varepsilon=0} = \int \frac{\delta \mathcal{F}[q]}{\delta q(\mathbf{x})} \eta(\mathbf{x}) d\mathbf{x}$ , we extract the functional derivative directly from the integrand.  $\square$

**Lemma 2.** *Let  $\mathcal{F}$  be a functional depending on an initial density  $q_0$  through an intermediate time-evolved density  $q_t$ . The chain rule for functional derivatives states that:*

$$\frac{\delta \mathcal{F}[q_t[q_0]]}{\delta q_0(\mathbf{x}_0)} = \int \frac{\delta \mathcal{F}[q_t]}{\delta q_t(\mathbf{x})} \frac{\delta q_t[q_0](\mathbf{x})}{\delta q_0(\mathbf{x}_0)} d\mathbf{x}.$$

*Proof.* See Appendix A of [49].  $\square$

**Lemma 3.** *Let  $\{\rho_t\}_t$  be a generic sequence of marginal distributions and  $\Phi_\rho(t, s, \cdot)$  be its associated PF-ODE flow map. Under a stop-gradient—where the spatial derivative of the score function is treated as zero—the Jacobian of the flow map simplifies to a scaled identity matrix:*

$$D_{\mathbf{x}_s} \Phi_\rho(t, s, \mathbf{x}_s) = c(s, t)I, \quad \text{where} \quad c(s, t) = \exp \left( \int_s^t a(u) du \right).$$

*Proof.* For simplicity, let  $J_t := D_{\mathbf{x}_s} \Phi_\rho(t, s, \mathbf{x}_s) = D_{\mathbf{x}_s} \mathbf{x}_t$  denote the Jacobian of the flow map from initial time  $s$  to time  $t$ . Differentiating with respect to time  $t$  gives  $\frac{dJ_t}{dt} = D_{\mathbf{x}_s} \left( \frac{d\mathbf{x}_t}{dt} \right)$ . Substituting the PF-ODE results in the following.

$$\frac{dJ_t}{dt} = D_{\mathbf{x}_s} \left( a(t)\mathbf{x}_t - \frac{1}{2}g(t)^2 \nabla_{\mathbf{x}_t} \log \rho_t(\mathbf{x}_t) \right).$$

For the first term,  $D_{\mathbf{x}_s} (a(t)\mathbf{x}_t) = a(t)J_t$ . For the second term, the multivariate chain rule gives:

$$D_{\mathbf{x}_s} (\nabla_{\mathbf{x}_t} \log \rho_t(\mathbf{x}_t)) = D_{\mathbf{x}_t} (\nabla_{\mathbf{x}_t} \log \rho_t(\mathbf{x}_t)) J_t.$$

Enforcing the stop-gradient strictly zeroes out the spatial derivative of the score function, eliminating the second term. The differential equation simplifies to  $\frac{dJ_t}{dt} = a(t)J_t$ . Given  $J_s = I$ , solving this linear ODE directly gives  $J_t = \exp \left( \int_s^t a(u) du \right) I = c(s, t)I$ .  $\square$

**Lemma 4.** *The functional derivative of the evolved density  $q_t(\mathbf{x})$  with respect to the initial density  $q_0(\mathbf{x}_0)$  is given by the following:*

$$\frac{\delta q_t[q_0](\mathbf{x})}{\delta q_0(\mathbf{x}_0)} = C(t) \delta(\mathbf{x}_0 - \Phi_q(0, t, \mathbf{x})),$$

where  $C(t) = c(t, 0)^d = \exp \left( -d \int_0^t a(s) ds \right)$ .

*Proof.* The marginal  $q_t$  is the pushforward of  $q_0$  under  $\Phi_q(t, 0, \cdot)$ . By the change of variables formula:

$$q_t(\mathbf{x}) = q_0(\Phi_q(0, t, \mathbf{x})) |\det D_{\mathbf{x}} \Phi_q(0, t, \mathbf{x})|.$$

From Lemma 3, the Jacobian is  $D_{\mathbf{x}} \Phi_q(0, t, \mathbf{x}) = c(t, 0)I$ , with determinant  $c(t, 0)^d = C(t)$ . Substituting this scaling factor into the density relation yields:

$$q_t(\mathbf{x}) = C(t) q_0(\Phi_q(0, t, \mathbf{x})).$$

Using the sifting property of the Dirac delta function, we can rewrite this as:

$$q_t(\mathbf{x}) = \int C(t) q_0(\mathbf{y}) \delta(\mathbf{y} - \Phi_q(0, t, \mathbf{x})) d\mathbf{y}.$$

Taking the functional derivative with respect to  $q_0$  evaluated at  $\mathbf{x}_0$  gives:

$$\frac{\delta q_t[q_0](\mathbf{x})}{\delta q_0(\mathbf{x}_0)} = C(t) \int \frac{\delta q_0(\mathbf{y})}{\delta q_0(\mathbf{x}_0)} \delta(\mathbf{y} - \Phi_q(0, t, \mathbf{x})) d\mathbf{y}.$$

Since  $\frac{\delta q_0(\mathbf{y})}{\delta q_0(\mathbf{x}_0)} = \delta(\mathbf{y} - \mathbf{x}_0)$ , the integral collapses to  $C(t) \delta(\mathbf{x}_0 - \Phi_q(0, t, \mathbf{x}))$ .  $\square$

**Functional Derivative of KL divergence.** We now evaluate the functional derivative of the KL divergence. Applying Lemma 2, we substitute the results from Lemma 1 and Lemma 4:

$$\frac{\delta D_{\text{KL}}[q_t[q_0]]}{\delta q_0(\mathbf{x}_0)} = \int \left( \log \frac{q_t(\mathbf{x})}{p_t(\mathbf{x})} + 1 \right) C(t) \delta(\mathbf{x}_0 - \Phi_q(0, t, \mathbf{x})) d\mathbf{x}.$$

We perform a change of variables  $\mathbf{y} = \Phi_q(0, t, \mathbf{x})$ . The Jacobian determinant of this mapping is exactly  $C(t)$ , giving  $d\mathbf{x} = C(t)^{-1}d\mathbf{y}$ . Substituting this transformation,  $C(t)$  perfectly cancels:

$$\frac{\delta D_{\text{KL}}[q_t[q_0]]}{\delta q_0(\mathbf{x}_0)} = \int \left( \log \frac{q_t(\Phi_q(t, 0, \mathbf{y}))}{p_t(\Phi_q(t, 0, \mathbf{y}))} + 1 \right) \delta(\mathbf{x}_0 - \mathbf{y}) d\mathbf{y}.$$

This simplifies to:

$$\frac{\delta D_{\text{KL}}[q_t[q_0]]}{\delta q_0(\mathbf{x}_0)} = \log \left( \frac{q_t(\mathbf{x}_t)}{p_t(\mathbf{x}_t)} \right) + 1.$$

**Putting It All Together.** The objective functional is given by  $\mathcal{F}[q_0] = \mathbb{E}_{t \sim \mathcal{U}[0, T]} [w(t) D_{\text{KL}}(q_t \| p_t)]$ , with weighting function:

$$w(t) = \frac{1}{2}(T - t)g(t)^2 c(t, 0)^2.$$

By the linearity of the functional derivative, substituting our previous result gives:

$$\frac{\delta \mathcal{F}[q_0]}{\delta q_0(\mathbf{x}_0)} = \mathbb{E}_t \left[ w(t) \left( \log \frac{q_t(\mathbf{x}_t)}{p_t(\mathbf{x}_t)} + 1 \right) \right].$$

To derive the Wasserstein gradient, we take the spatial gradient with respect to the initial state  $\mathbf{x}_0$ . Passing the gradient operator through the expectation and applying the spatial chain rule, we have  $\nabla_{\mathbf{x}_0} = (D_{\mathbf{x}_0} \mathbf{x}_t)^T \nabla_{\mathbf{x}_t}$ . Using Lemma 3, the forward flow Jacobian reduces to  $D_{\mathbf{x}_0} \mathbf{x}_t = c(0, t)I$ , giving us:

$$\nabla_{\mathbf{x}_0} \frac{\delta \mathcal{F}[q_0]}{\delta q_0(\mathbf{x}_0)} = \mathbb{E}_t \left[ w(t) c(0, t) \nabla_{\mathbf{x}_t} \log \frac{q_t}{p_t}(\mathbf{x}_t) \right].$$

Substituting the explicit form of  $w(t)$  and applying the inverse relation  $c(t, 0) = c(0, t)^{-1}$ , the expression simplifies to:

$$\nabla_{\mathbf{x}_0} \frac{\delta \mathcal{F}[q_0]}{\delta q_0(\mathbf{x}_0)} = \mathbb{E}_t \left[ \frac{1}{2}(T - t)g(t)^2 c(t, 0) \nabla_{\mathbf{x}_t} \log \frac{q_t}{p_t}(\mathbf{x}_t) \right].$$

## A.2 Expected Gradient Direction

We now demonstrate that the PFD gradient  $\mathbb{E}_t[\Delta_t(\mathbf{x}_0)]$ , where  $\Delta_t(\mathbf{x}_0) = \mathbf{x}_0 - \hat{\mathbf{x}}_0$ , exactly matches the Wasserstein gradient derived above. This requires the following preliminary result.

**Lemma 5.** Consider a flow map  $\Phi(t, s, \mathbf{x})$  governed by the generic differential equation  $\frac{d\mathbf{x}}{d\tau} = \mathbf{F}(\mathbf{x}, \tau)$ . The partial derivative of this map with respect to its initial time  $s$  satisfies the following:

$$\partial_s \Phi(t, s, \mathbf{x}) = -D_{\mathbf{x}} \Phi(t, s, \mathbf{x}) \mathbf{F}(\mathbf{x}, s).$$

*Proof.* See Chapter 5 of [50]. □

**Deriving an Expression for the Gradient Estimator.** We have  $\hat{\mathbf{x}}_0(t) = \Phi_p(0, t, \mathbf{x}_t)$ . Differentiating this composition with respect to the sampled time  $t$  gives:

$$\frac{d}{dt} \hat{\mathbf{x}}_0 = \partial_t \Phi_p(0, t, \mathbf{x}_t) + D_{\mathbf{x}_t} \Phi_p(0, t, \mathbf{x}_t) \dot{\mathbf{x}}_t.$$

Applying Lemma 5 to the derivative  $\partial_t \Phi_p$  and substituting the vector field of the pre-trained prior's PF-ODE, we get the following expression:

$$\partial_t \Phi_p(0, t, \mathbf{x}_t) = -D_{\mathbf{x}_t} \Phi_p(0, t, \mathbf{x}_t) \left[ \mathbf{f}(\mathbf{x}_t, t) - \frac{1}{2}g(t)^2 \nabla_{\mathbf{x}_t} \log p_t(\mathbf{x}_t) \right].$$

Concurrently, the forward trajectory  $\mathbf{x}_t$  is governed by the generation PF-ODE:  $\dot{\mathbf{x}}_t = \mathbf{f}(\mathbf{x}_t, t) - \frac{1}{2}g(t)^2 \nabla_{\mathbf{x}_t} \log q_t(\mathbf{x}_t)$ . Substituting these expressions back into the total time derivative of  $\hat{\mathbf{x}}_0$  results in:

$$\begin{aligned} \frac{d}{dt} \hat{\mathbf{x}}_0 &= D_{\mathbf{x}_t} \Phi_p(0, t, \mathbf{x}_t) \left[ \left( \mathbf{f}(\mathbf{x}_t, t) - \frac{1}{2}g(t)^2 \nabla_{\mathbf{x}_t} \log q_t(\mathbf{x}_t) \right) \right. \\ &\quad \left. - \left( \mathbf{f}(\mathbf{x}_t, t) - \frac{1}{2}g(t)^2 \nabla_{\mathbf{x}_t} \log p_t(\mathbf{x}_t) \right) \right]. \end{aligned}$$

The drift terms  $\mathbf{f}(\mathbf{x}_t, t)$  cancel identically. Moreover, under the applied stop-gradient, using Lemma 3, the Jacobian of the reverse flow simplifies to the scalar matrix  $D_{\mathbf{x}_t} \Phi_p(0, t, \mathbf{x}_t) = c(t, 0)I$ . Taking this into account, we arrive at the following.

$$\frac{d}{dt} \hat{\mathbf{x}}_0 = -\frac{1}{2}c(t, 0)g(t)^2 \nabla_{\mathbf{x}_t} \log \frac{q_t(\mathbf{x}_t)}{p_t(\mathbf{x}_t)}.$$

Since  $\mathbf{x}_0$  is independent of  $t$ , its derivative with respect to it vanishes. Consequently, the derivative of  $\Delta_t$  with respect to  $t$  is simply the negation of the reconstruction's derivative:

$$\frac{d}{dt} \Delta_t = -\frac{d}{dt} \hat{\mathbf{x}}_0 = \frac{1}{2}c(t, 0)g(t)^2 \nabla_{\mathbf{x}_t} \log \frac{q_t(\mathbf{x}_t)}{p_t(\mathbf{x}_t)}.$$

Integrating this from time 0 to  $t$ , and using the boundary condition  $\Delta_0 = 0$ , which follows from  $\hat{\mathbf{x}}_0(0) = \Phi_p(0, 0, \mathbf{x}_0) = \mathbf{x}_0$ , gives us the following expression for the gradient estimator:

$$\Delta_t = \int_0^t \frac{1}{2}c(s, 0)g(s)^2 \nabla_{\mathbf{x}_s} \log \frac{q_s(\mathbf{x}_s)}{p_s(\mathbf{x}_s)} ds.$$

**Final Gradient.** To compute the expected discrepancy, we integrate over uniformly sampled random times  $t \sim \mathcal{U}(0, T)$ :

$$\mathbb{E}_t[\Delta_t] = \frac{1}{T} \int_0^T \left( \int_0^t \frac{1}{2}c(s, 0)g(s)^2 \nabla_{\mathbf{x}_s} \log \frac{q_s(\mathbf{x}_s)}{p_s(\mathbf{x}_s)} ds \right) dt.$$

We apply Fubini's theorem to exchange the order of integration over the triangular domain  $0 \leq s \leq t \leq T$ . By integrating first with respect to  $t$ , we obtain:

$$\mathbb{E}_t[\Delta_t] = \frac{1}{T} \int_0^T \left( \int_s^T dt \right) \frac{1}{2}c(s, 0)g(s)^2 \nabla_{\mathbf{x}_s} \log \frac{q_s(\mathbf{x}_s)}{p_s(\mathbf{x}_s)} ds.$$

Evaluating the straightforward inner integral  $\int_s^T dt = (T - s)$  simplifies the expression to:

$$\mathbb{E}_t[\Delta_t] = \frac{1}{T} \int_0^T \frac{1}{2}(T - s)c(s, 0)g(s)^2 \nabla_{\mathbf{x}_s} \log \frac{q_s(\mathbf{x}_s)}{p_s(\mathbf{x}_s)} ds.$$

Recognizing this as an expectation over the uniform distribution  $t \sim \mathcal{U}(0, T)$ , we arrive at our final expression for the gradient:

$$\mathbb{E}_t[\Delta_t] = \mathbb{E}_{t \sim \mathcal{U}[0, T]} \left[ \frac{1}{2}(T - t)g(t)^2 c(t, 0) \nabla_{\mathbf{x}_t} \log \frac{q_t(\mathbf{x}_t)}{p_t(\mathbf{x}_t)} \right].$$

This result is algebraically identical to the Wasserstein gradient  $\nabla_{\mathbf{x}_0} \frac{\delta \mathcal{F}[q_0]}{\delta q_0(\mathbf{x}_0)}$  derived in the Appendix A.1. Therefore, we conclude that the negative gradient  $\mathbb{E}_t[\Delta_t]$  provides the exact velocity field required to perform Wasserstein gradient descent on the time-averaged KL divergence functional, thus promoting distribution matching. ■

## B PFD Algorithm

We summarize here the PFD algorithm as an iterative particle-based optimization procedure. Let  $q_0^\tau$  denote the empirical distribution of particles at iteration  $\tau$ . The operators  $\Phi_{q^\tau}^\rightarrow(\cdot, t)$  and  $\Phi_p^\leftarrow(\cdot, t)$  denote the solutions of the forward and reverse PF-ODEs associated with the current distribution  $\{q_t^\tau\}_t$  and the target diffusion prior  $\{p_t\}_t$ , respectively.

---

### Algorithm 1 Probability-Flow Distillation

---

```

1: Input:  $\{\mathbf{x}_0^{(i)}\}_{i=1}^N, \tau_{\max}, \eta$  // particle ensemble, iterations, learning rate
2:  $\tau \leftarrow 0$  // initialize iteration
3: while  $\tau < \tau_{\max}$  and not converged do // stopping criterion
4:    $\mathbf{x}_0 \sim q_0^\tau, t \sim \mathcal{U}(0, T)$  // sample particle and time
5:    $\mathbf{x}_t \leftarrow \Phi_{q^\tau}^\rightarrow(\mathbf{x}_0, t)$  // forward PF-ODE
6:    $\hat{\mathbf{x}}_0 \leftarrow \Phi_p^\leftarrow(\mathbf{x}_t, t)$  // reverse PF-ODE
7:    $\Delta_t \leftarrow \mathbf{x}_0 - \hat{\mathbf{x}}_0$  // gradient estimator
8:    $\mathbf{x}_0 \leftarrow \mathbf{x}_0 - \eta \Delta_t$  // particle update
9:    $\tau \leftarrow \tau + 1$  // increment iteration
10: end while
11: Output:  $\{\mathbf{x}_0^{(i)}\}_{i=1}^N$  // optimized particle ensemble

```

---

## C Derivation of the Reparameterized DDIM PF-ODE

**The PF-ODE associated with VP-SDE.** For the VP-SDE, the drift term is given by  $\mathbf{f}(\mathbf{x}, t) = -\frac{1}{2}\beta_t \mathbf{x}$  with diffusion coefficient  $g(t) = \sqrt{\beta_t}$ . The corresponding PF-ODE is, therefore, given by

$$\frac{d\mathbf{x}_t}{dt} = -\frac{1}{2}\beta_t \mathbf{x}_t - \frac{1}{2}\beta_t \nabla_{\mathbf{x}} \log p_t(\mathbf{x}_t).$$

By applying the standard substitution for the score function in terms of the predicted noise  $\epsilon_\phi(\mathbf{x}_t, t)$ :  $\nabla_{\mathbf{x}} \log p_t(\mathbf{x}_t) = -\frac{\epsilon_\phi(\mathbf{x}_t, t)}{\sqrt{1-\alpha_t}}$ , the ODE can be rewritten in its noise-conditioned form:

$$\frac{d\mathbf{x}_t}{dt} = -\frac{1}{2}\beta_t \mathbf{x}_t + \frac{1}{2} \frac{\beta_t}{\sqrt{1-\alpha_t}} \epsilon_\phi(\mathbf{x}_t, t).$$

**Change of Variables.** Next, we apply the change of variables  $\tilde{\mathbf{x}}_t = \frac{\mathbf{x}_t}{\sqrt{\alpha_t}}$ . Taking the derivative with respect to time  $t$  results in:

$$\frac{d\tilde{\mathbf{x}}_t}{dt} = \frac{1}{\sqrt{\alpha_t}} \frac{d\mathbf{x}_t}{dt} - \frac{1}{2} \frac{\dot{\alpha}_t}{\alpha_t} \tilde{\mathbf{x}}_t.$$

Substituting the ODE equation from above and the relation  $\dot{\alpha}_t = -\beta_t \alpha_t$  causes the  $\tilde{\mathbf{x}}_t$  terms to perfectly cancel, leaving:

$$\frac{d\tilde{\mathbf{x}}_t}{dt} = \frac{1}{2} \frac{\beta_t}{\sqrt{\alpha_t(1-\alpha_t)}} \epsilon_\phi(\mathbf{x}_t, t).$$

**Reparameterization in  $\sigma$ .** To connect this to the signal-to-noise ratio, we differentiate  $\sigma_t = \sqrt{\frac{1-\alpha_t}{\alpha_t}}$  with respect to  $t$ :

$$\frac{d\sigma_t}{dt} = \frac{1}{2} \frac{1}{\sigma_t} \frac{d}{dt} \left( \frac{1-\alpha_t}{\alpha_t} \right) = -\frac{1}{2} \frac{1}{\sigma_t} \frac{1}{\alpha_t} \frac{\dot{\alpha}_t}{\alpha_t} = \frac{1}{2} \frac{1}{\sigma_t} \frac{\beta_t}{\alpha_t} = \frac{1}{2} \frac{\beta_t}{\sqrt{\alpha_t(1-\alpha_t)}}.$$

Thus, giving rise to the simplified reparameterized DDIM PF-ODE:

$$\frac{d\tilde{\mathbf{x}}_t}{dt} = \epsilon_\phi(\mathbf{x}_t, t) \frac{d\sigma_t}{dt}.$$

Finally, rearranging the initial definition  $\tilde{\mathbf{x}}_t = \frac{\mathbf{x}_t}{\sqrt{\alpha_t}}$  and using the identity  $\alpha_t = \frac{1}{1+\sigma_t^2}$ , we can recover the unscaled state:

$$\mathbf{x}_t = \frac{\tilde{\mathbf{x}}_t}{\sqrt{1+\sigma_t^2}}.$$

## D Implementation Details

We implement our method in threestudio [51]—a modular framework for text-to-3D generation via distillation—and evaluate against its provided baseline implementations.

### D.1 3D Generation with PFD

**Representation and Initialization.** We instantiate PFD using a NeRF-based representation with a progressive hash-grid encoding [8]. The encoding employs 16 levels with 2 features per level, a base resolution of 16, and a per-level scale factor of 1.447, resulting in a maximum resolution of 4096. Higher-frequency levels are progressively activated beginning from level 8 (resolution  $\sim 200$ ), with only lower-frequency levels enabled during the first 1000 iterations and an additional level activated every 572 iterations thereafter, so that all levels become active by approximately 5k iterations. This coarse-to-fine schedule improves geometric smoothness.

Following Magic3D [13], we initialize the density field using  $\sigma_{\text{init}}(\boldsymbol{\mu}) = \lambda_{\sigma} \left(1 - \frac{\|\boldsymbol{\mu}\|_2^2}{r}\right)$ , with  $\lambda_{\sigma} = 10$  and  $r = 0.5$ . The camera radius is sampled from  $\mathcal{U}(1.0, 1.5)$ , and the scene is normalized within a bounding box of size 1.0. We employ a simple material model with sigmoid-activated RGB outputs together with a neural environment-map background.

**Diffusion Model and Solver.** We use Stable Diffusion 2.1-base [2] as the underlying text-to-image diffusion model. The DDIM-ODE is solved in both forward and reverse directions using the deterministic DPM++ solver [52], a higher-order numerical solver, with a time-dependent discretization consisting of  $\lfloor 10t/T \rfloor$  steps. We employ a CFG scale of 7.5 during the reverse process and  $-6.5$  during the forward process (See Section 4.2 and Appendix E.2).

**Optimization.** We optimize for 7.5k iterations using Adam with learning rates of  $10^{-2}$  for geometry parameters and  $10^{-3}$  for background parameters. The sampling time range is annealed from  $[0.02T, 0.98T]$  to  $[0.02T, 0.70T]$  after 7k iterations, improving texture refinement during later stages of optimization. All experiments are conducted on a single NVIDIA A100 GPU with 80 GB VRAM, requiring approximately two hours per generated object.

### D.2 Baselines

For SDS, we use DeepFloyd IF [53] as the underlying diffusion model, following the recommendations in the threestudio repository, and run it with the default hyperparameters for 10k iterations. For SDI and CSD, we retain the default configurations provided in threestudio, including the additional components and multistage optimizations proposed by the respective authors. For VSD, which also consists of multiple stages, we compare only against the first stage, as it corresponds most closely to the setting considered by PFD, while the subsequent stages primarily perform additional geometry and texture refinement and incur substantially higher computational cost. Consequently, we restrict VSD to 10k iterations, with the sampling time range annealed from  $[0.02T, 0.98T]$  to  $[0.02T, 0.50T]$  after 5k iterations. We additionally employ the single-particle setting, which is the only configuration currently supported by threestudio and is consistent with the single-particle adaptation of PFD for text-to-3D generation.

### D.3 Licenses

Table 2: Licenses of models and libraries used in this work.

Component	License
Stable Diffusion 2.1-base [2]	CreativeML Open RAIL++-M License
DeepFloyd IF [53]	DeepFloyd IF License
ThreeStudio [51]	Apache License 2.0
HuggingFace Diffusers [54]	Apache License 2.0

## E Ablation Study

### E.1 Effect of the Proposed Improvement

We evaluate the effect of the proposed improvement by comparing PFD against SDI—the baseline method upon which our approach builds—under identical settings, with time annealing disabled and no additional regularization applied. Qualitative results are shown in Figure 6. At low resolution ( $64 \times 64$ , Figure 6(a,c)), PFD already produces more visually appealing textures with richer fine-grained detail compared to SDI. At higher resolution ( $512 \times 512$ , Figure 6(b,d)), this gap becomes even more pronounced, with PFD generating more natural-looking details and substantially improved perceptual texture quality.

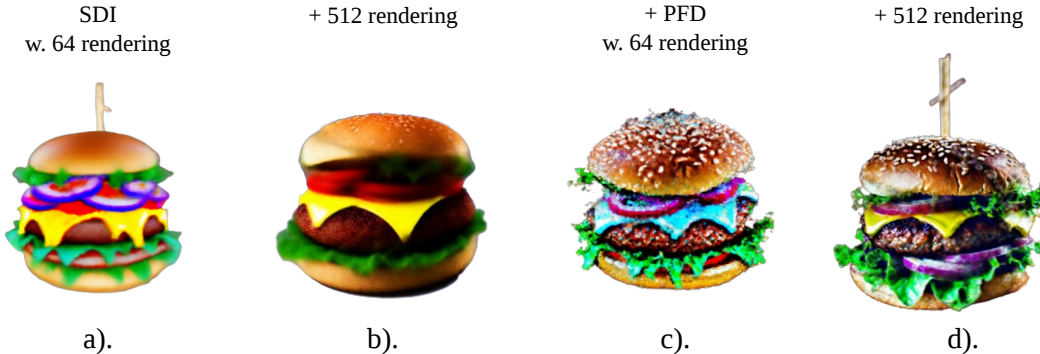


Figure 6: (a,b) SDI at  $64 \times 64$  and  $512 \times 512$ , (c,d) PFD at  $64 \times 64$  and  $512 \times 512$

### E.2 Effect of the CFG Scale

**Observation at varying scales.** We analyze the effect of the CFG scale on generation quality. As the guidance scale increases, the generated outputs become increasingly noisy and distorted (see Figure 7). This behavior arises because larger guidance scales amplify the guidance term, making the discretized DDIM-ODE less stable during optimization. In practice, moderate guidance scales in the range of 5 to 12 provide a good balance between convergence speed and prompt alignment without causing instability. Accordingly, we use a CFG scale of 7.5 in all experiments.

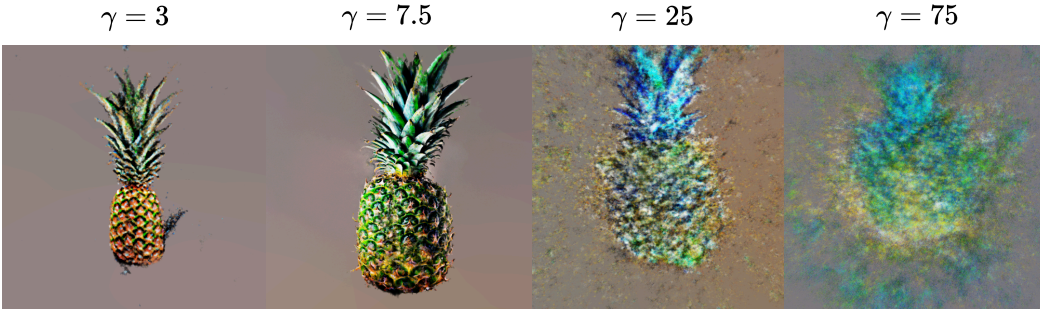


Figure 7: Effect of increasing CFG scale  $\gamma$ . As  $\gamma$  increases, the generated results become progressively distorted.

**Negative CFG for DDIM Inversion.** We further study the role of negative CFG in the forward process. As discussed in Section 4.2, a negative CFG is required to correctly reverse the source and target distributions, as it provides an estimate of the score of the source marginals  $\{q_t^T\}_t$ . Figure 8 shows results for different sign combinations. Using a negative sign in the forward process and a positive sign in the reverse process results in coherent generations, whereas other combinations lead to degraded outputs with artifacts.

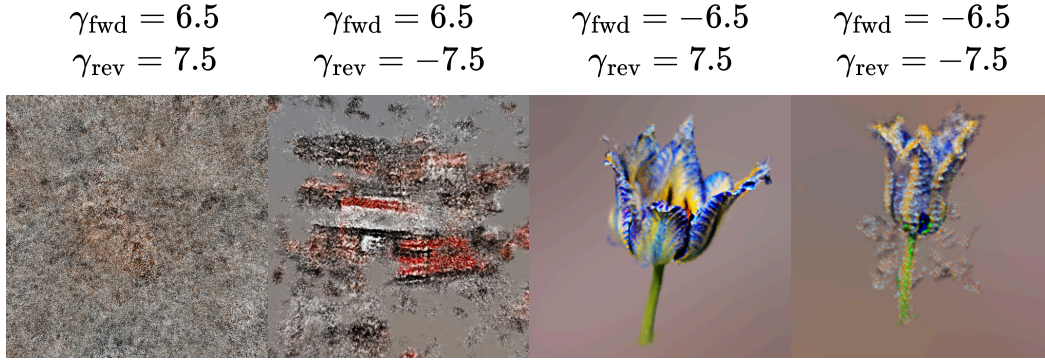


Figure 8: Effect of forward and reverse CFG scales  $(\gamma_{\text{fwd}}, \gamma_{\text{rev}})$ .

### E.3 Effect of Time Annealing

We study the effect of time annealing on generation quality. Early in optimization, sampling across a wide range of  $t$  encourages global alignment between  $q_t^{\bar{}}$  and  $p_t$ . During later stages ( $\tau > 7000$ ), we anneal the sampling range toward smaller values of  $t$ , focusing optimization on lower-noise regimes and high-frequency details. As shown in Figure 9, this improves texture quality and produces cleaner colors compared to using a fixed time range.



Figure 9: Effect of time annealing during late-stage optimization on generated 3D assets.

## F Janus Failure Mode

A common failure mode in text-to-3D generation via distillation is the Janus problem, where multiple faces or object identities are fused into a single geometry, as shown in Figure 10. In the mouse bust example, the face is repeated across different sides of the geometry, producing conflicting frontal structures. In the hotdog example, two distinct dog faces emerge within the same object under different viewpoints.



Figure 10: Illustration of the Janus problem. Generated 3D objects exhibit inconsistent geometry across viewpoints.

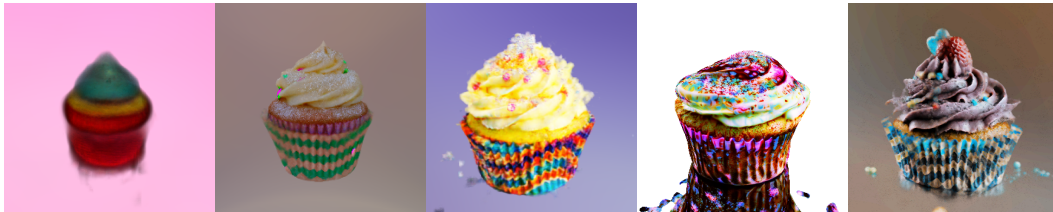
## G Additional Qualitative Results



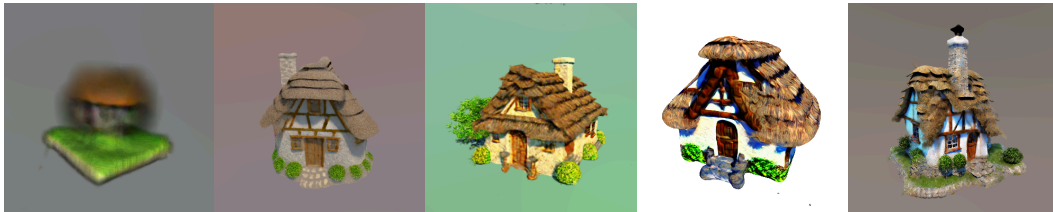
"A baby bunny sitting on a stack of pancakes."



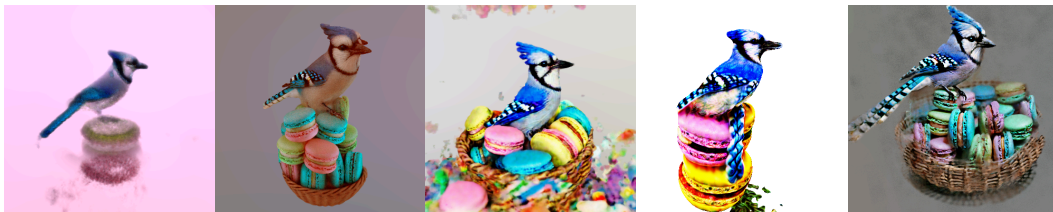
"A DSLR photograph of a hamburger."



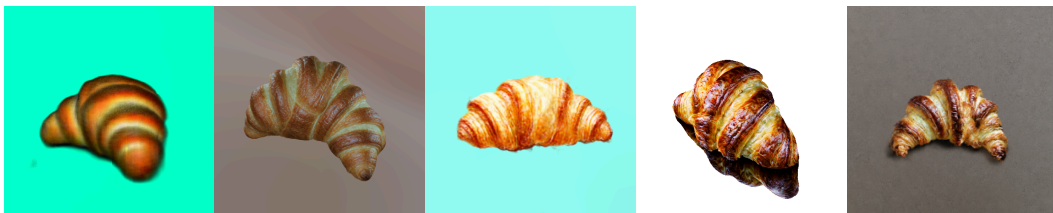
"A DSLR photograph of a beautifully decorated cupcake."



"A 3D model of an adorable cottage with thatched roof."



"A blue jay standing on a large basket of rainbow macarons."



"A delicious croissant."

SDS

SDI

VSD

CSD

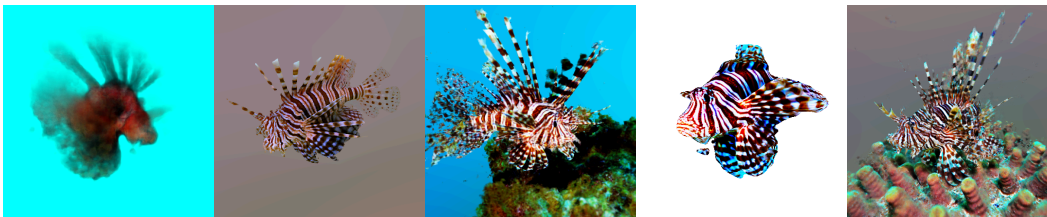
PFD (Ours)



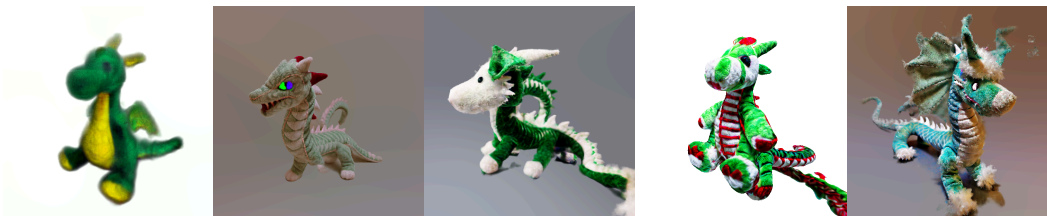
*"A pineapple."*



*"A stack of pancakes covered in maple syrup."*



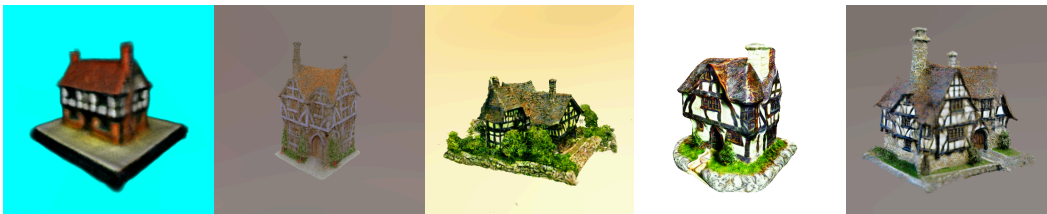
*"A lionfish."*



*"A plush dragon toy."*



*"A moss covered rock with small fibers sticking out."*



*"A model of a house in Tudor style."*

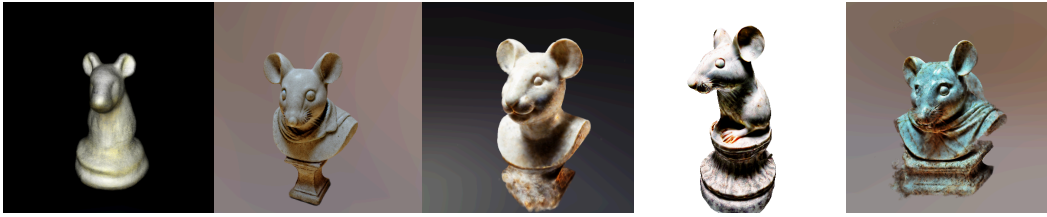
SDS

SDI

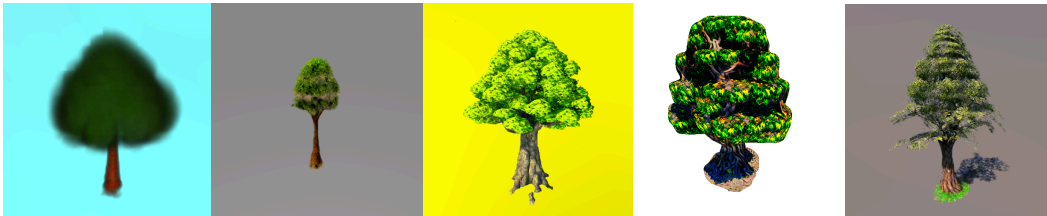
VSD

CSD

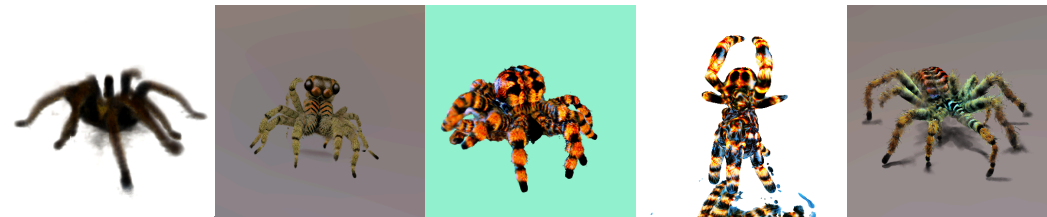
PFD (Ours)



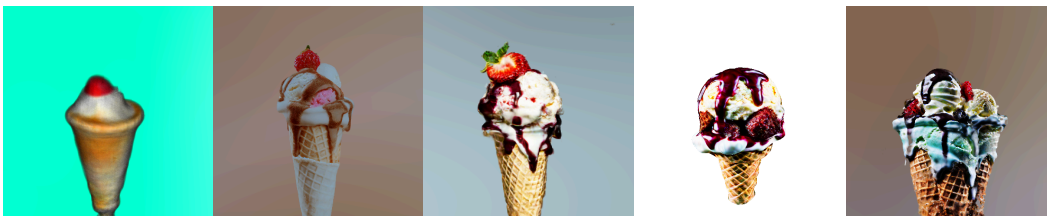
"A marble bust of a mouse."



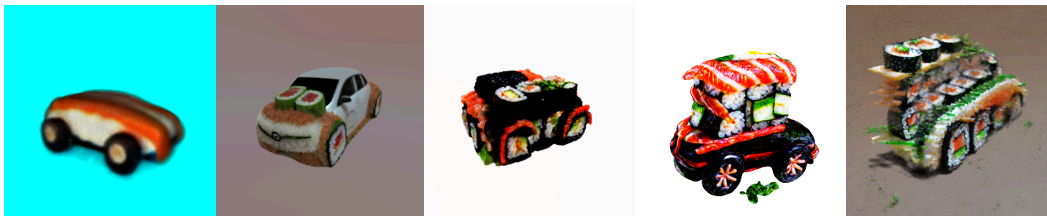
"A highly detailed tree."



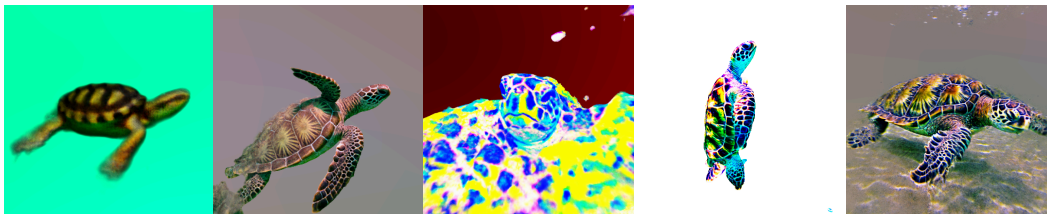
"A tarantula, highly detailed."



"A high quality photo of an icecream sundae."



"A car made out of sushi."



"A zoomed in DSLR photograph of a sea turtle."